

3-21-2014

Investigation of the High-Temperature Redox Chemistry of $\text{Sr}_2\text{Fe}_{1.5}\text{Mo}_{0.5}\text{O}_{6-\delta}$ via *In Situ* Neutron Diffraction

Daniel E. Bugaris

Jason P. Hodges


Ashfia Hug

W. Michael Chance

Andreas Heyden
heyden@cec.sc.edu

See next page for additional authors

Follow this and additional works at: https://scholarcommons.sc.edu/emec_facpub

 Part of the [Applied Mechanics Commons](#), and the [Materials Science and Engineering Commons](#)

Publication Info

Published in *Journal of Materials Chemistry A*, Volume 2, Issue 11, 2014, pages 4045-4054.

This Article is brought to you by the Mechanical Engineering, Department of at Scholar Commons. It has been accepted for inclusion in Faculty Publications by an authorized administrator of Scholar Commons. For more information, please contact digres@mailbox.sc.edu.

Author(s)

Daniel E. Bugaris, Jason P. Hodges, Ashfia Hug, W. Michael Chance, Andreas Heyden, Fanglin Chen, and Hans-Conrad zur Loye

Cite this: *J. Mater. Chem. A*, 2014, 2, 4045

Investigation of the high-temperature redox chemistry of $\text{Sr}_2\text{Fe}_{1.5}\text{Mo}_{0.5}\text{O}_{6-\delta}$ via *in situ* neutron diffraction†

Daniel E. Bugaris,^a Jason P. Hodges,^b Ashfia Huq,^b W. Michael Chance,^a Andreas Heyden,^c Fanglin Chen^d and Hans-Conrad zur Loye^{*a}

Crystallographic structural changes were investigated for $\text{Sr}_2\text{Fe}_{1.5}\text{Mo}_{0.5}\text{O}_{6-\delta}$, an electrode material for symmetric solid oxide fuel cells. The samples of this material were heated and cooled in wet hydrogen and wet oxygen atmospheres, to simulate the reducing and oxidizing conditions experienced under actual fuel cell operating conditions, and their structures and oxygen contents were determined using *in situ* powder neutron diffraction. The existence of a reversible tetragonal to cubic phase transition was established to occur between room temperature and 400 °C, both on heating and cooling in either oxygen or hydrogen. The oxygen content reaches a low value of 5.50(2) at 850 °C in wet hydrogen. Excellent correlations are observed between the oxygen content of the structure and the conductivities reported in the literature.

Received 27th November 2013
Accepted 26th January 2014

DOI: 10.1039/c3ta14913g

www.rsc.org/MaterialsA

1 Introduction

Solid oxide fuel cells (SOFCs) have garnered much attention for their ability to directly convert chemical energy into electrical power with high conversion efficiency.^{1–3} Current SOFCs continue to be based on yttria-stabilized zirconia (YSZ) coupled with a porous Ni-YSZ cermet anode that performs well in hydrogen and CO-based fuels. However, the presence of Ni leads to coking when exposed to hydrocarbon-based fuels, and also the operational temperature of Ni-YSZ is very high which has disadvantages in materials choices, sealing mechanisms, *etc.* In efforts to improve SOFCs with fuel flexibility, different materials have been investigated. For example, perovskite-based systems became of great interest after the publications by Goodenough on $\text{Sr}_2\text{MgMoO}_{6-\delta}$ ^{4,5} that prompted researchers to investigate related systems.^{6–8} Recently, $\text{Sr}_2\text{Fe}_{1.5}\text{Mo}_{0.5}\text{O}_{6-\delta}$ (SFM) was identified as a promising candidate for SOFCs due to its high conductivity of 10–20 S cm^{−1} at 800 °C in either a reducing or an oxidizing atmosphere.^{9–11} There is a renewed interest in

this family of compounds for use in SOFCs, in particular after it was discovered that it could function as both anode and cathode in a symmetrical fuel cell architecture.⁸ In a symmetrical SOFC, the anode and cathode consist of the same material, which is beneficial because it is believed that this can be an effective approach to create a fuel cell tolerant of the detrimental effects of sulfur poisoning and coking of the electrodes as it allows for the *in situ* regeneration of the electrodes when the fuel cell is reversed.^{12,13} Furthermore, since both cathode and anode are the same, the symmetrical fuel cell architecture reduces the number of unique components as well as eliminating one electrode/electrolyte interface. To be suitable candidates for SOFCs such electrode materials have to be stable under both oxidizing and reducing conditions, have high electronic and ionic conductivity, and maintain significant catalytic activity for oxygen reduction and hydrogen oxidation. An additional challenge is the ability to minimize reactions between the electrode and the electrolyte. An investigation of its reactivity demonstrated that $\text{Sr}_2\text{Fe}_{1.5}\text{Mo}_{0.5}\text{O}_{6-\delta}$ is chemically stable at elevated temperatures in the presence of standard electrolytes such as $\text{La}_{0.9}\text{Sr}_{0.1}\text{Ga}_{0.8}\text{Mg}_{0.2}\text{O}_3$ (LSGM), $\text{Sm}_{0.2}\text{Ce}_{0.8}\text{O}_{1.95}$ (SDC),¹⁴ and $\text{BaZr}_{0.1}\text{Ce}_{0.7}\text{Y}_{0.2}\text{O}_{3-\delta}$ (BZCY).⁸ $\text{Sr}_2\text{Fe}_{1.5}\text{Mo}_{0.5}\text{O}_{6-\delta}$ is stable in wet hydrogen and oxygen and SFM/LSGM/SFM systems can achieve power densities in excess of 800 mW cm² in wet H₂ and over 200 mW cm² in CH₄ at 900 °C.⁸ Finally, it has been shown that SFM can be regenerated after sulfur poisoning and after coking, demonstrating that this is indeed a very exciting electrode material for symmetrical fuel cells.⁸

As far as the cation composition is concerned, symmetrical fuel cells have identical anode and cathode materials. However, since the anode is exposed to reducing conditions and the

^aDepartment of Chemistry and Biochemistry, University of South Carolina, Columbia, SC 29208, USA. E-mail: zurloye@mailbox.sc.edu; Tel: +1 803 777 6916

^bNeutron Sciences Directorate, Oak Ridge National Laboratory, Oak Ridge, TN 37831, USA

^cDepartment of Chemical Engineering, University of South Carolina, Columbia, SC 29208, USA

^dDepartment of Mechanical Engineering, University of South Carolina, Columbia, SC 29208, USA

† Electronic supplementary information (ESI) available: Powder neutron diffraction profiles for $\text{Sr}_2\text{Fe}_{1.5}\text{Mo}_{0.5}\text{O}_{6-\delta}$ during cooling from 850 °C in O₂, as well as afterwards at room temperature in a sealed vanadium canister. See DOI: 10.1039/c3ta14913g

cathode to oxidizing conditions, we expect an appreciable difference in their oxygen contents. Furthermore, the change in oxygen content can have an effect on the crystal structure of the material and different structural modifications can be thermodynamically stable or kinetically trapped over a range of oxygen contents.

The Sr–Fe–Mo–O system has garnered interest not only for its application in fuel cells, but also for very complex magnetic and electronic properties.^{2,15,16} For these reasons, a number of groups have investigated the structures and compositions of the Sr–Fe–Mo–O system under a range of environmental conditions. It should be noted that these phases have been prepared by a variety of techniques, including sol–gel synthesis and standard solid-state reactions. $\text{Sr}_2\text{Fe}_x\text{Mo}_{2-x}\text{O}_{6-\delta}$ ($0.8 < x < 1.5$) was investigated by Rao *et al.*, who explored the structure as a function of iron content. They established that this system is stable over a wide range of cation compositions and associated oxygen contents.¹⁷ The system was reported to crystallize in the double perovskite structure in the tetragonal space group $I4/mmm$ over most of this composition range; however, for $x > 1.2$, the system adopted a cubic structure in space group $Fm\bar{3}m$. The iron and molybdenum atoms were found to partially order in the double perovskite structure ($\text{A}_2\text{BB}'\text{O}_6$) due to the size and charge difference; however, for the iron to molybdenum ratio of 3 : 1, $\text{Sr}_2\text{Fe}_{1.5}\text{Mo}_{0.5}\text{O}_{6-\delta}$, the iron–molybdenum ordering ceases and both atoms are randomly distributed over the B and B' sites. In a related study, Meneghini *et al.* reported the presence of anti-site defects and suggested that samples can retain a degree of very short-range order while macroscopically appearing to be fully disordered.¹⁸

It has recently been established that the structures belonging to the Sr–Fe–Mo–O system are very sensitive to the synthetic conditions and, in particular, the resulting oxygen content, which has a significant influence on the structure of the material. A powder X-ray diffraction study that tracked the structure of $\text{Sr}_2\text{Fe}_{1.5}\text{Mo}_{0.5}\text{O}_{6-\delta}$ as a function of temperature found that a good fit was obtained using either the cubic space group $Fm\bar{3}m$ with $a = 7.8575(1)$ Å in a double perovskite setting, or the cubic space group $Pm\bar{3}m$ with $a = 3.9287(1)$ Å when refined as a simple perovskite structure (ABO_3) due to the absence of iron–molybdenum ordering on the two crystallographic B/B' sites.¹² The structure remained cubic up to 800 °C, with no indication of a structural change. The same $\text{Sr}_2\text{Fe}_{1.5}\text{Mo}_{0.5}\text{O}_{6-\delta}$ composition, however, prepared *via* an innovative microwave synthesis, was refined by powder neutron diffraction in the orthorhombic space group $Pnma$, which generated a better refinement than either the cubic or tetragonal space groups.¹⁹ Once again, no iron–molybdenum ordering was observed. The structure of the same $\text{Sr}_2\text{Fe}_{1.5}\text{Mo}_{0.5}\text{O}_{6-\delta}$ composition (prepared *via* a sol–gel synthesis) was also refined in the tetragonal space group $I4/mcm$ with $a = 5.54301(15)$ Å and $c = 7.8471(4)$ Å using powder neutron diffraction, supported by electron diffraction data.¹⁵ No iron–molybdenum ordering was reported in this case either.

To correlate structure and properties of SOFC materials, it is crucial to understand the structural evolution of these compounds under actual fuel cell operating conditions. Thus we have used variable temperature, *in situ* powder neutron

diffraction in highly reducing and highly oxidizing conditions to study the structural behavior of $\text{Sr}_2\text{Fe}_{1.5}\text{Mo}_{0.5}\text{O}_{6-\delta}$. Neutrons offer distinct advantages over X-ray diffraction for structural studies.^{20–22} Here, the synthesis of $\text{Sr}_2\text{Fe}_{1.5}\text{Mo}_{0.5}\text{O}_{6-\delta}$ and its complete structural characterization by high temperature powder neutron diffraction under oxidizing and reducing conditions is presented.

2 Experimental

A powder sample of $\text{Sr}_2\text{Fe}_{1.5}\text{Mo}_{0.5}\text{O}_{6-\delta}$ was prepared by a previously reported procedure.¹⁹ The starting reagents were SrCO_3 (Aldrich, 99.9+%), Fe_2O_3 (Alfa Aesar, 99.5%), and MoO_3 (Alfa Aesar, 99.95%). SrCO_3 was dried overnight at 150 °C to remove any water. The remaining reagents were used as received. Initially, $\text{Fe}_2(\text{MoO}_4)_3$ was synthesized from a 1 : 3 stoichiometric mixture of Fe_2O_3 and MoO_3 . The powders were ground thoroughly with a mortar and pestle before being placed in an alumina boat, which was heated in a furnace at 12 °C min^{-1} to 750 °C and held for 12 h, before turning off the furnace and cooling to room temperature. The phase purity of $\text{Fe}_2(\text{MoO}_4)_3$ was confirmed by powder X-ray diffraction. The diffraction data were collected on a Rigaku Ultima IV powder diffractometer with a high speed D/teX Ultra detector using $\text{Cu K}\alpha$ radiation; the data were collected over the 2θ range 10–80° with a scan speed of 10° min^{-1} . All of the peaks in the powder pattern could be indexed in the monoclinic space group $P2_1$ with lattice parameters matching those reported in the literature for $\text{Fe}_2(\text{MoO}_4)_3$. In the second step of the preparation of $\text{Sr}_2\text{Fe}_{1.5}\text{Mo}_{0.5}\text{O}_{6-\delta}$, a stoichiometric ratio of SrCO_3 , Fe_2O_3 , and $\text{Fe}_2(\text{MoO}_4)_3$ was thoroughly ground with a mortar and pestle, before being placed in an alumina boat. The reaction mixture was heated in a furnace at 12 °C min^{-1} to 1000 °C, where it was held for 12 h, followed by quickly cooling to room temperature. The sample was then re-ground, placed in an alumina boat, and heated in 5 h to 1200 °C, where it was held for 12 h before furnace cooling to room temperature. This process was repeated 10 times with intermittent re-grinding of the sample, and the progress of the reaction was tracked by powder X-ray diffraction. The reaction was deemed complete when the powder pattern of the sample could be indexed by the reported tetragonal space group $I4/mcm$ with nearly equivalent lattice parameters, and no impurity phases (e.g. SrMoO_4).

Time-of-flight (TOF) powder neutron diffraction data were collected using the POWGEN (BL-11A) diffractometer at the Spallation Neutron Source, Oak Ridge National Laboratory, Oak Ridge, Tennessee. Two samples of $\text{Sr}_2\text{Fe}_{1.5}\text{Mo}_{0.5}\text{O}_{6-\delta}$ with masses of 3.761 g and 3.012 g, respectively, were loaded into separate 6 mm diameter quartz baskets with porous silica frit bottoms. The first sample was loaded into a temperature and atmosphere controlled furnace, and neutron diffraction data were collected at 58 °C while the instrument was purged with N_2 . The data were collected using a center wavelength of 1.333 Å and corresponding d -spacing range 0.41–3.6 Å. The input gas was then switched to a 4% H_2 –96% He mixture that was bubbled through H_2O before entering the instrument to ensure proper humidity ($p\text{O}_2 = 10^{-16}$ atm). Once the gas had

thoroughly purged the instrument, the furnace was rapidly heated to 400 °C, and after allowing the temperature to equilibrate sufficiently, diffraction data were collected. This process was then repeated for the following temperatures: 500 °C, 600 °C, 700 °C, 750 °C, 800 °C, and 850 °C. As the furnace was cooled in intervals, diffraction data were collected at the same temperatures down to 400 °C. Upon reaching room temperature, the input gas was switched to N₂ to purge the instrument, and the sample was removed. The second sample was loaded into the same furnace and after purging with N₂, the input gas was switched to O₂ that was also bubbled through H₂O in order to again ensure proper humidity. Once the instrument had been purged, the furnace was rapidly heated to 850 °C. Upon stabilization of the temperature, diffraction data were collected. The furnace was then gradually cooled, stopping at the following temperatures to collect diffraction data: 800 °C, 700 °C, 600 °C, and 500 °C. After reaching room temperature, the input gas was switched to N₂ to purge the instrument, and the sample was removed. At a later time, both samples (H₂- and O₂-treated) were loaded into 6 mm diameter vanadium canisters. Diffraction data were collected at room temperature with two different center wavelengths of 1.333 Å and 3.731 Å, corresponding to the *d*-spacing ranges 0.4–3.6 Å and 1.66–8.24 Å, respectively. Rietveld refinement of the data was performed using the GSAS software package and the EXPGUI interface.^{23,24} TOF peak-profile function number 3 (tabulated peak-shape dependency determined by use of NIST SRM-660b LaB₆ powder) and the reciprocal interpolation function were used for modeling the diffraction peaks and background, respectively. For the temperatures 58 °C, 400 °C, 600 °C, 700 °C, and 750 °C of the *in situ* diffraction data collections, alumel, chromel, and inconel were refined as additional phases due to contributions from the thermocouple during the data collections. For the room temperature data collections, vanadium (sample canister) was refined as an additional phase.

3 Results and discussion

Sr₂Fe_{1.5}Mo_{0.5}O_{6-δ} has proven to be an important electrode material for SOFCs and has been incorporated into symmetrical fuel cell structures.⁸ Due to its excellent performance, it is desirable to better understand the structure of this material not only at room temperature but also at high temperatures and, more importantly, to understand how the structure and composition change under actual fuel cell operating conditions. To date, several groups have investigated the structure and, at room temperature, have refined the material in one of several space groups, including cubic *Fm* $\bar{3}$ *m* and *Pm* $\bar{3}$ *m*, tetragonal *I4/mcm* and *I4/mmm*, and orthorhombic *Pnma*. In several cases, electron diffraction studies were performed that supported specific space group choices. DFT + *U* calculations indicate that the cubic structure is the most stable, consistent with what we observe at elevated temperatures.¹⁹ The discrepancies in the structure refinements between different groups are most likely due to the differences in the sample preparation methods and associated oxygen contents of the samples. The observed compositions can range from full oxygen site occupancy

(Sr₂Fe_{1.5}Mo_{0.5}O₆) to partial oxygen site occupancy (Sr₂Fe_{1.5}Mo_{0.5}O_{5.5}). The different preparation methods used, importantly, affect not only the composition, but also the metal oxidation states, which are tied to the oxygen content. The change in cation size as a function of oxygen content is an additional factor that can impact the structure and space group of the prepared material.

The initial structure refinement of Sr₂Fe_{1.5}Mo_{0.5}O_{6-δ} was done with neutron diffraction data collected at 58 °C. The best Rietveld refinement of the data set was obtained in the tetragonal space group *I4/mcm* with full oxygen occupancy to yield a composition of Sr₂Fe_{1.5}Mo_{0.5}O₆ (Table 1 and Fig. 1 and 2). This result is qualitatively in excellent agreement with the work published by Retuerto *et al.*, who refined a sample of Sr₂Fe_{1.5}Mo_{0.5}O_{6-δ} in the same space group; however, they found the material to be slightly oxygen deficient on the O1 position, while the O2 position was stoichiometric.¹⁵ Clearly the precise synthetic conditions are important as different preparative approaches can lead to different sample compositions and,

Table 1 Structural parameters and interatomic distances/angles for Sr₂Fe_{1.5}Mo_{0.5}O_{6-δ} in tetragonal space group *I4/mcm* from *in situ* powder neutron diffraction while purging in N₂. Three phases are used in the refinement in order to accommodate the unusual strain broadening observed in the peaks

<i>T</i> (°C)	58	58	58
Phase	1	2	3
Wt fraction	0.14(1)	0.661(7)	0.195(5)
<i>a</i> (Å)	5.5548(2)	5.5540(1)	5.5372(6)
<i>c</i> (Å)	7.8783(5)	7.8414(3)	7.8052(8)
Sr 4b (0, 1/2, 1/4)			
<i>U</i> _{iso} (Å ²)	0.0163(2)	0.0163(2)	0.0163(2)
<i>f</i> _{occ}	1.00	1.00	1.00
(Fe–Mo) 4c (0, 0, 0)			
<i>U</i> _{iso} (Å ²)	0.0112(2)	0.0112(2)	0.0112(2)
<i>f</i> _{occ}	1.00	1.00	1.00
O1 16k (<i>x</i> , <i>y</i> , 0)			
<i>x</i>	0.2371(3)	0.2371(3)	0.2371(3)
<i>y</i>	0.7371(3)	0.7371(3)	0.7371(3)
<i>U</i> ₁₁ (Å ²)	0.0153(8)	0.0153(8)	0.0153(8)
<i>U</i> ₂₂ (Å ²)	0.0153(8)	0.0153(8)	0.0153(8)
<i>U</i> ₃₃ (Å ²)	0.022(1)	0.022(1)	0.022(1)
<i>f</i> _{occ}	1.00	1.00	1.00
O2 4a (0, 0, 1/4)			
<i>U</i> ₁₁ (Å ²)	0.025(2)	0.025(2)	0.025(2)
<i>U</i> ₂₂ (Å ²)	0.025(2)	0.025(2)	0.025(2)
<i>U</i> ₃₃ (Å ²)	0.013(1)	0.013(1)	0.013(1)
<i>f</i> _{occ}	1.00	1.00	1.00
χ ²	3.181	3.181	3.181
<i>R</i> _p (%)	9.52	9.52	9.52
<i>R</i> _{wp} (%)	5.27	5.27	5.27
Distances (Å)			
Fe–Mo–O1 (<i>x</i> ₄)	1.9665(2)	1.9663(1)	1.9603(3)
Fe–Mo–O2 (<i>x</i> ₂)	1.9696(1)	1.9603(1)	1.9513(2)
Average Fe–Mo–O	1.9675(4)	1.9643(2)	1.9573(7)
Angles (°)			
O1–Fe/Mo–O1	90.000	90.000	90.000
O1–Fe/Mo–O1	180.000	180.000	180.000
O1–Fe/Mo–O2	90.000	90.000	90.000
O2–Fe/Mo–O2	180.000	180.000	180.000

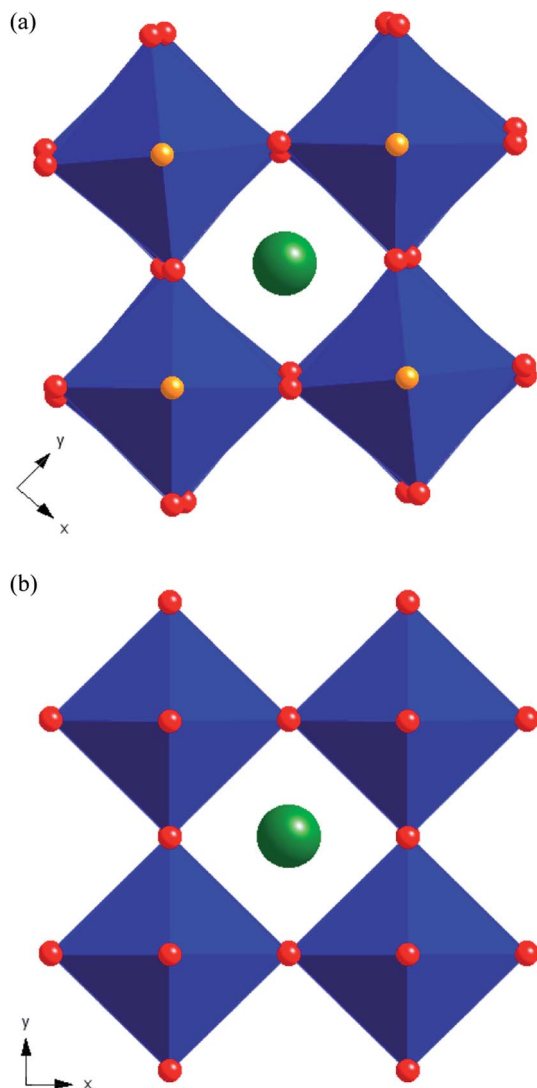


Fig. 1 View of the (a) tetragonal and (b) cubic crystal structures of $\text{Sr}_2\text{Fe}_{1.5}\text{Mo}_{0.5}\text{O}_{6-\delta}$. Sr atoms are shown as green spheres and $(\text{Fe}/\text{Mo})\text{O}_6$ octahedra are shown in blue. In the tetragonal structure, equatorial oxygen atoms (atomic position O(1)) are shown as red spheres, and axial oxygen atoms (atomic position O(2)) are shown as orange spheres. In the cubic structure, there is only one oxygen atomic position, which is shown with red spheres.

hence, refinement solutions for both X-ray and neutron diffraction data.

The sample environment was changed to 4% hydrogen in helium, hydrated by bubbling the gas mixture through water prior to introducing it to the sample. This created an atmosphere with a $p\text{O}_2 = 10^{-16}$ atm, as measured by an in-line oxygen sensor (which is connected to the exhaust stream of the gas from the sample). The sample was heated in steps to a final temperature of 850 °C and data were collected at 400 °C, 500 °C, 600 °C, 700 °C, 750 °C, 800 °C, and 850 °C (Fig. 3 and 4) after allowing one hour for sample equilibration at each temperature. To ensure that the sample had fully equilibrated at each temperature, the data were sectioned into 5 minute slices and sequential slices were compared to each other. Once the

diffraction patterns for adjacent slices were identical within experimental error, the remaining slices were summed and used for the structure refinement at each temperature. This process takes advantage of the time event data format utilized at all SNS scattering instruments. The refinement results are summarized in Table 2. The best refinements for all data sets collected at elevated temperatures (400 °C and up) were carried out in the cubic space group $Pm\bar{3}m$, indicating that $\text{Sr}_2\text{Fe}_{1.5}\text{Mo}_{0.5}\text{O}_6$ undergoes a structural transition from tetragonal to cubic between 58 °C and 400 °C without a measurable change in oxygen content. We attempted to use differential thermal analysis (DTA) measurements to establish the transition temperature, but were unable to detect a definitive signal. As the structural change is minor between the $I4/mcm$ and $Pm\bar{3}m$ symmetries, involving only a slight motion of the oxygen atoms, our inability to establish the transition temperature by thermal methods is not surprising. Once the sample has transitioned to the cubic space group, the structure remains cubic at least up to 850 °C, the highest measured temperature.

The oxygen content of $\text{Sr}_2\text{Fe}_{1.5}\text{Mo}_{0.5}\text{O}_{6-\delta}$ heated in a wet 4% H_2 atmosphere ($p\text{O}_2 = 10^{-16}$ atm) starts to decrease beginning at 500 °C, $\text{Sr}_2\text{Fe}_{1.5}\text{Mo}_{0.5}\text{O}_{5.78}$, and almost linearly decreases to higher temperatures, reaching $\text{Sr}_2\text{Fe}_{1.5}\text{Mo}_{0.5}\text{O}_{5.5}$ at 850 °C (Table 2). The cubic lattice parameter, a , increases from 3.9444(1) Å at 400 °C to 3.9794(1) Å at 850 °C, most likely due to a combination of the thermal expansion of the structure and the overall reduction in the metal cation oxidation states resulting in a concomitant increase in the cation sizes.

Cooling the sample in the same reducing atmosphere ($p\text{O}_2 = 10^{-16}$ atm) results in an increase in the sample's oxygen content (Table 3). The source of the oxygen is the water vapor from the wet hydrogen atmosphere. The oxygen content, however, does not exactly mirror the values during the heating process, but remains slightly lower, such that even at 400 °C, there is a persistent oxygen deficiency with a refined sample composition of $\text{Sr}_2\text{Fe}_{1.5}\text{Mo}_{0.5}\text{O}_{5.78}$. The sample's crystallographic symmetry, however, remains cubic, as expected. Only by cooling the sample slowly back down to room temperature is the full oxygen occupancy restored, along with a structural transition back to the $I4/mcm$ space group (Table 4 and Fig. 5).

The second half of the original sample was heated to 850 °C in a pure oxygen atmosphere and then cooled back down to 500 °C. The tetragonal to cubic transition takes place below 500 °C also in pure oxygen, such that the structure again was refined as cubic between 850 °C and 500 °C. Data were collected at 850 °C, 800 °C, 700 °C, 600 °C, and 500 °C (Table 5 and Fig. S1 and S2†). The sample was equilibrated at each temperature for 1 hour and, as before, tested for having reached equilibrium by analyzing adjacent 5 minute data slices. It is interesting to note that even in pure oxygen, the sample is not fully oxidized at 850 °C and exhibits a refined composition of $\text{Sr}_2\text{Fe}_{1.5}\text{Mo}_{0.5}\text{O}_{5.85}$. On cooling, the oxygen content of the sample increased as expected and full oxygen occupancy was reached by 700 °C and remained invariant down to 400 °C. Slowly cooling the sample to room temperature in oxygen results in the structural transition from the cubic space group $Pm\bar{3}m$ to the tetragonal space group $I4/mcm$ (Table 6 and Fig. S3†).

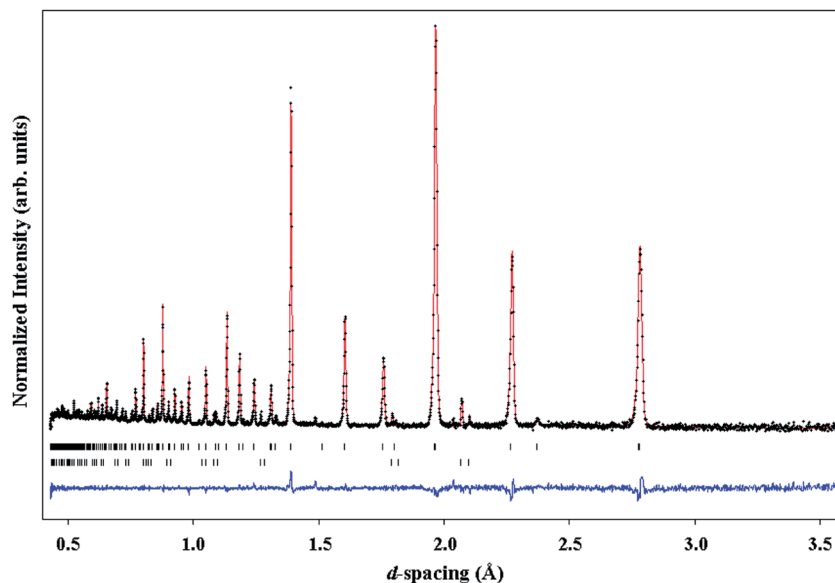


Fig. 2 Observed (black crosses), calculated (red line), and difference (blue line) powder neutron diffraction profile for $\text{Sr}_2\text{Fe}_{1.5}\text{Mo}_{0.5}\text{O}_{6-\delta}$ in N_2 at 58°C , refined in the tetragonal space group $I4/mcm$. The vertical markers correspond to the allowed Bragg reflections for $\text{Sr}_2\text{Fe}_{1.5}\text{Mo}_{0.5}\text{O}_6$ (upper) and the thermocouple (lower) composed of alumel, chromel, and inconel.

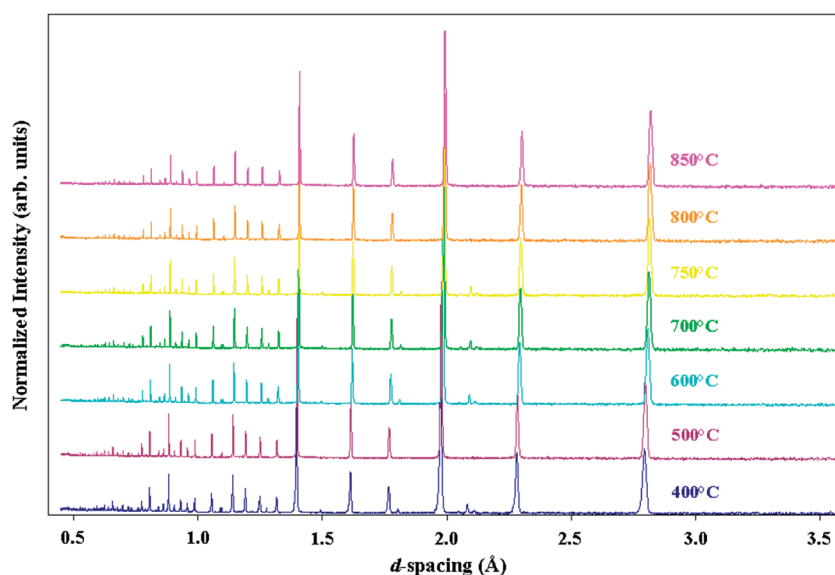


Fig. 3 Powder neutron diffraction profiles for $\text{Sr}_2\text{Fe}_{1.5}\text{Mo}_{0.5}\text{O}_{6-\delta}$ in 4% H_2 –96% He in the temperature range 400 – 850°C .

At room temperature $\text{Sr}_2\text{Fe}_{1.5}\text{Mo}_{0.5}\text{O}_{6-\delta}$ is tetragonal and can persist in the tetragonal structure over a range of oxygen contents. This suggests that the phase transition is not significantly affected by the sample's oxygen content, at least over the reported compositional range of $\text{Sr}_2\text{Fe}_{1.5}\text{Mo}_{0.5}\text{O}_6$ to $\text{Sr}_2\text{Fe}_{1.5}\text{Mo}_{0.5}\text{O}_{5.92(2)}$, although it is likely, and supported by reports in the literature, that for more significant oxygen deficiencies, the cubic phase can be kinetically trapped down to room temperature. Clearly, the compositional space where the $I4/mcm$ structure is stable is extensive. The structural transition takes place in the absence of oxygen loss, and hence is not directly tied to the oxygen content, although one might expect the

oxygen content to potentially affect the specific temperature where the transition takes place.

In the perovskite family of ABO_3 oxides, structural transitions are ubiquitous and are typically explained *via* the Goldschmidt tolerance factor, t , defined by $t = \frac{r_A + r_O}{\sqrt{2}(r_B + r_O)}$, where r_A , r_B , and r_O are the ionic radii of the respective ions.²⁵ For $t \sim 1$, the perovskite structure is expected to be cubic, while for smaller values of t , the structure will distort and become tetragonal or monoclinic. In the case of a double perovskite, $\text{A}_2\text{BB}'\text{O}_6$, such as $\text{Sr}_2\text{Fe}_{1.5}\text{Mo}_{0.5}\text{O}_6$, $r_{\text{BB}'}$, the average value of r_B and $r_{B'}$ is used instead of r_B , and the equation changes to

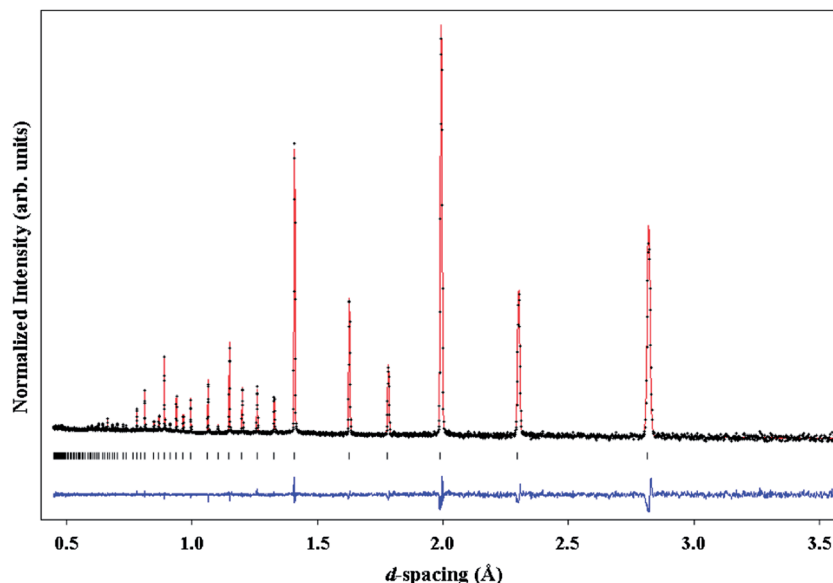


Fig. 4 Observed (black crosses), calculated (red line), and difference (blue line) powder neutron diffraction profile for $\text{Sr}_2\text{Fe}_{1.5}\text{Mo}_{0.5}\text{O}_{6-\delta}$ in 4% H_2 –96% He at 850 °C, refined in the cubic space group $Pm\bar{3}m$. The vertical markers correspond to the allowed Bragg reflections.

Table 2 Structural parameters and interatomic distances/angles for $\text{Sr}_2\text{Fe}_{1.5}\text{Mo}_{0.5}\text{O}_{6-\delta}$ in cubic space group $Pm\bar{3}m$ from *in situ* powder neutron diffraction at a selected temperature while heating in 4% H_2 –96% He

T (°C)	400	500	600	700	750	800	850
a (Å)	3.9444(1)	3.9586(1)	3.9637(1)	3.9696(1)	3.9727(1)	3.9760(1)	3.9794(1)
Sr 1b (1/2, 1/2, 1/2)							
U_{iso} (Å ²)	0.0249(3)	0.0300(2)	0.0337(2)	0.0357(2)	0.0378(2)	0.0391(3)	0.0411(3)
f_{occ}	1.00	1.00	1.00	1.00	1.00	1.00	1.00
Fe–Mo 1a (0, 0, 0)							
U_{iso} (Å ²)	0.0170(2)	0.0229(2)	0.0259(1)	0.0273(2)	0.0288(2)	0.0305(2)	0.0322(2)
f_{occ}	1.00	1.00	1.00	1.00	1.00	1.00	1.00
O1 3d (0, 0, 1/2)							
U_{11} (Å ²)	0.0344(4)	0.0443(3)	0.0504(2)	0.0528(4)	0.0543(4)	0.0568(4)	0.0591(5)
U_{22} (Å ²)	0.0344(4)	0.0443(3)	0.0504(2)	0.0528(4)	0.0543(4)	0.0568(4)	0.0591(5)
U_{33} (Å ²)	0.0169(6)	0.0203(4)	0.0203(3)	0.220(4)	0.0245(5)	0.0254(5)	0.0263(5)
f_{occ}	1.00	0.964(3)	0.960(2)	0.950(3)	0.933(3)	0.930(4)	0.916(4)
χ^2	10.95	3.653					
R_p (%)	12.50	8.79	8.41	9.51	10.86	9.77	10.26
R_{wp} (%)	9.57	5.57	5.30	6.00	6.40	5.17	5.60
Distances (Å)							
Fe–Mo–O (x_6)	1.9722(1)	1.9793(1)	1.9819(1)	1.9848(1)	1.9864(1)	1.9880(1)	1.9897(1)
Angles (°)							
O–Fe/Mo–O	90.000	90.000	90.000	90.000	90.000	90.000	90.000
O–Fe/Mo–O	180.000	180.000	180.000	180.000	180.000	180.000	180.000

$t = \frac{r_A + r_O}{\sqrt{2}(r_{\text{BB}'} + r_O)}$. Almost all perovskites have t values ranging from 0.75–1.1 and it is generally true that perovskites with roughly $t = 0.98$ to 1.07 are cubic, those with $t = 0.97$ to 0.99 are tetragonal, and those with $t = 0.86$ to 0.96 are monoclinic.²⁶

Our neutron diffraction data indicate that $\text{Sr}_2\text{Fe}_{1.5}\text{Mo}_{0.5}\text{O}_6$ is tetragonal at room temperature and becomes cubic by 400 °C. The tolerance factor for $\text{Sr}_2\text{Fe}_{1.5}\text{Mo}_{0.5}\text{O}_6$, $t = 0.99$ assuming all Mo^{+6} and $(\text{Fe}^{+3}/\text{Fe}^{+4})$, is within both the cubic and tetragonal stability range and consistent with our neutron diffraction results of the tetragonal space group $I4/mcm$. Our neutron

diffraction measurements as a function of temperature demonstrate that by 400 °C, and with continued full oxygen occupancy, the structure undergoes a phase change to the cubic $Pm\bar{3}m$ space group. This structural transition is most likely driven by the thermal expansion of the unit cell, pushing $\text{Sr}_2\text{Fe}_{1.5}\text{Mo}_{0.5}\text{O}_6$ from tetragonal to cubic. This is not surprising given the tolerance factor of $\text{Sr}_2\text{Fe}_{1.5}\text{Mo}_{0.5}\text{O}_6$.

As the sample is heated to 850 °C in wet hydrogen, the oxygen content drops to a composition of $\text{Sr}_2\text{Fe}_{1.5}\text{Mo}_{0.5}\text{O}_{5.5}$. If we assume that this results in a reduction of Mo^{6+} to Mo^{5+} and all iron to Fe^{3+} , then we obtain a tolerance factor of $t = 0.988$,

Table 3 Structural parameters and interatomic distances/angles for $\text{Sr}_2\text{Fe}_{1.5}\text{Mo}_{0.5}\text{O}_{6-\delta}$ in cubic space group $Pm\bar{3}m$ from *in situ* powder neutron diffraction at a selected temperature while cooling in 4% H_2 –96% He

T (°C)	800	750	700	600	500	400
a (Å)	3.9763(1)	3.9731(1)	3.9700(1)	3.9640(1)	3.9583(1)	3.9525(1)
Sr 1b (1/2, 1/2, 1/2)						
U_{iso} (Å ²)	0.0385(4)	0.0365(4)	0.0353(3)	0.0321(3)	0.0289(3)	0.0266(3)
f_{occ}	1.00	1.00	1.00	1.00	1.00	1.00
Fe–Mo 1a (0, 0, 0)						
U_{iso} (Å ²)	0.0300(3)	0.0287(3)	0.0271(3)	0.0246(3)	0.0223(3)	0.0201(2)
f_{occ}	1.00	1.00	1.00	1.00	1.00	1.00
O1 3d (0, 0, 1/2)						
U_{11} (Å ²)	0.0564(7)	0.0550(6)	0.0523(6)	0.0492(5)	0.0450(5)	0.0417(4)
U_{22} (Å ²)	0.0564(7)	0.0550(6)	0.0523(6)	0.0492(5)	0.0450(5)	0.0417(4)
U_{33} (Å ²)	0.0241(8)	0.0230(7)	0.0220(7)	0.0190(6)	0.0188(6)	0.0172(6)
f_{occ}	0.928(6)	0.938(5)	0.941(5)	0.955(5)	0.960(5)	0.963(5)
χ^2	1.364					
R_p (%)	17.35	17.89	17.71	17.29	17.11	17.23
R_{wp} (%)	9.14	10.13	9.84	9.65	9.37	10.08
Distances (Å)						
Fe–Mo–O (x_6)	1.9882(1)	1.9865(1)	1.9850(1)	1.9820(1)	1.9791(1)	1.9763(1)
Angles (°)						
O–Fe/Mo–O	90.000	90.000	90.000	90.000	90.000	90.000
O–Fe/Mo–O	180.000	180.000	180.000	180.000	180.000	180.000

Table 4 Structural parameters and interatomic distances/angles for $\text{Sr}_2\text{Fe}_{1.5}\text{Mo}_{0.5}\text{O}_{6-\delta}$ in tetragonal space group $I4/mcm$ from powder neutron diffraction after cooling the sample in 4% H_2 –96% He

T (°C)	25
a (Å)	5.5631(1)
c (Å)	7.8730(1)
Sr 4b (0, 1/2, 1/4)	
U_{iso} (Å ²)	0.0135(1)
f_{occ}	1.00
(Fe–Mo) 4c (0, 0, 0)	
U_{iso} (Å ²)	0.0107(1)
f_{occ}	1.00
O1 16k (x, y, 0)	
x	0.2425(4)
y	0.7425(4)
U_{11} (Å ²)	0.0340(6)
U_{22} (Å ²)	0.0340(6)
U_{33} (Å ²)	0.0217(9)
f_{occ}	1.00
O2 4a (0, 0, 1/4)	
U_{11} (Å ²)	0.0205(8)
U_{22} (Å ²)	0.0205(8)
U_{33} (Å ²)	0.0045(8)
f_{occ}	1.00
χ^2	5.982
R_p (%)	10.22
R_{wp} (%)	5.06
Distances (Å)	
Fe–Mo–O1 (x_4)	1.9677(1)
Fe–Mo–O2 (x_2)	1.9683(1)
Average Fe–Mo–O	1.9679(2)
Angles (°)	
O1–Fe/Mo–O1	90.000
O1–Fe/Mo–O1	180.000
O1–Fe/Mo–O2	90.000
O2–Fe/Mo–O2	180.000

just slightly less than $t = 0.996$ for the fully oxidized phase and still within the cubic tolerance factor range. Again, the thermal expansion is expected to prevent the structure from reverting back to the tetragonal structure. Presumably, if $\text{Sr}_2\text{Fe}_{1.5}\text{Mo}_{0.5}\text{O}_{6-\delta}$ is cooled to room temperature quickly, the oxygen deficit can be retained and the cubic space group trapped at room temperature. This would be a kinetic effect, as the cubic sample at room temperature would not be in thermodynamic equilibrium. It is also conceivable that a rapid synthesis, such as the microwave heating method employed by Chen *et al.*, could kinetically trap even an orthorhombic structure. Based on many reports in the literature it is clear that the structure of this material is very sensitive to the preparation.

$\text{Sr}_2\text{Fe}_{1.5}\text{Mo}_{0.5}\text{O}_{6-\delta}$ exhibits high oxide ion conductivity in air (0.13 S cm^{−1} at 800 °C) with an activation energy of 83.3 kJ mol^{−1}.⁷ The total conductivity of $\text{Sr}_2\text{Fe}_{1.5}\text{Mo}_{0.5}\text{O}_{6-\delta}$ is a function of the surrounding atmosphere and temperature, which directly impact the structure and oxygen vacancy concentration. The conductivity has been measured and it was reported that under reducing conditions the conductivity of $\text{Sr}_2\text{Fe}_{1.5}\text{Mo}_{0.5}\text{O}_{6-\delta}$ increases from about 5 S cm^{−1} to roughly 14 S cm^{−1} between 475 °C and 800 °C in wet H_2 .¹¹ The total conductivity is a combination of the O^{2−} ionic conductivity and the electronic conductivity, which are influenced by the oxygen vacancy concentration and the oxidation states of the metals and the band structure. They are connected *via* the composition, yet of independent origins. To explain these two contributions to the overall conductivity, DFT + U calculations have been carried out.¹⁹ These published calculations were able to explain the high conductivity of $\text{Sr}_2\text{Fe}_{1.5}\text{Mo}_{0.5}\text{O}_{6-\delta}$ as well as the stability of the structure towards oxygen loss and concomitant vacancy formation. Furthermore, these calculations show that the high electronic conductivity arises from the hybridization of the Fe d

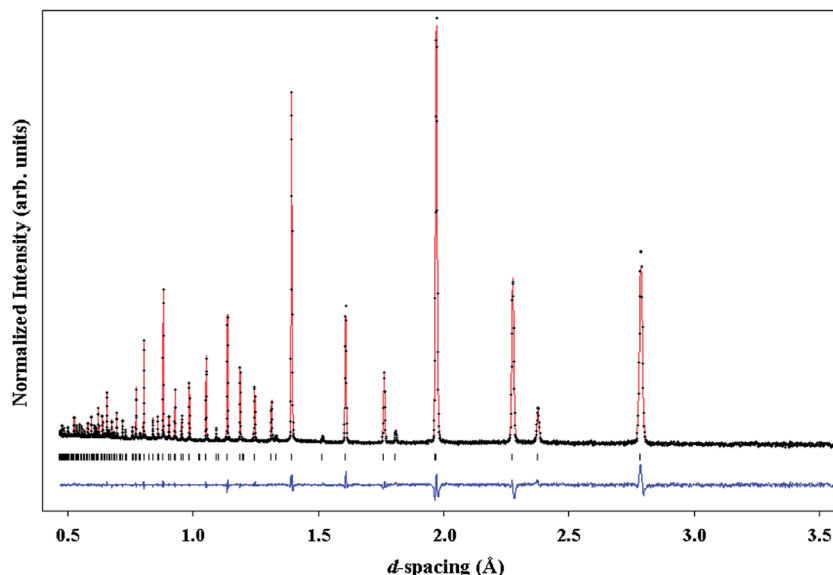


Fig. 5 Observed (black crosses), calculated (red line), and difference (blue line) powder neutron diffraction profile for $\text{Sr}_2\text{Fe}_{1.5}\text{Mo}_{0.5}\text{O}_{6-\delta}$ at 25 °C after having been cooled in 4% H_2 –96% He, refined in the tetragonal space group $I4/mcm$. The vertical markers correspond to the allowed Bragg reflections.

Table 5 Structural parameters and interatomic distances/angles for $\text{Sr}_2\text{Fe}_{1.5}\text{Mo}_{0.5}\text{O}_{6-\delta}$ in cubic space group $Pm\bar{3}m$ from *in situ* powder neutron diffraction at a selected temperature while cooling in O_2

T (°C)	850	800	700	600	500
a (Å)	3.9723(1)	3.9685(1)	3.9612(1)	3.9544(1)	3.9483(1)
Sr 1b (1/2, 1/2, 1/2)					
U_{iso} (Å ²)	0.0392(3)	0.0371(3)	0.0338(3)	0.0310(3)	0.0276(3)
f_{occ}	1.00	1.00	1.00	1.00	1.00
Fe–Mo 1a (0, 0, 0)					
U_{iso} (Å ²)	0.0280(2)	0.0265(2)	0.0234(2)	0.0215(2)	0.0189(2)
f_{occ}	1.00	1.00	1.00	1.00	1.00
O1 3d (0, 0, 1/2)					
U_{11} (Å ²)	0.0509(4)	0.0490(4)	0.0449(3)	0.0413(4)	0.0367(4)
U_{22} (Å ²)	0.0509(4)	0.0490(4)	0.0449(3)	0.0413(4)	0.0367(4)
U_{33} (Å ²)	0.0256(5)	0.0247(5)	0.0228(5)	0.0208(6)	0.0185(6)
f_{occ}	0.975(3)	0.988(3)	1.00	1.00	1.00
χ^2	4.305				
R_p (%)	8.36	8.54	9.82	12.67	12.10
R_{wp} (%)	5.24	5.45	6.97	8.26	8.26
Distances (Å)					
Fe–Mo–O (x_6)	1.9861(1)	1.9842(1)	1.9806(1)	1.9772(1)	1.9741(1)
Angles (°)					
O–Fe/Mo–O	90.000	90.000	90.000	90.000	90.000
O–Fe/Mo–O	180.000	180.000	180.000	180.000	180.000

and O p states and the creation of empty states across the Fermi level in the $\text{Sr}_2\text{Fe}_{1.5}\text{Mo}_{0.5}\text{O}_{6-\delta}$ conduction band, which are sustained even at high oxygen vacancy concentration. The same calculations attribute the high oxygen vacancy concentration to the very weak Fe–O bonds and the large charge delocalization that occurs when a neutral oxygen atom is removed. This electron delocalization upon oxygen vacancy formation favors the high conductivity observed in this material, as the empty states in the band structure can readily accommodate these delocalized charge carriers. It has been calculated that the electronic

conductivity, although tied to the vacancy concentration and electron delocalization, is not strongly affected by the vacancy concentration for smaller concentrations.

Our neutron diffraction data has determined the oxygen composition and space group of $\text{Sr}_2\text{Fe}_{1.5}\text{Mo}_{0.5}\text{O}_{6-\delta}$ as a function of temperature and oxygen partial pressure. Two types of oxygen vacancies can be present in this material, those between two adjacent iron atoms and those between an iron and a molybdenum atom. DFT + U calculations have shown that the former have a significantly lower formation energy because of the

Table 6 Structural parameters and interatomic distances/angles for $\text{Sr}_2\text{Fe}_{1.5}\text{Mo}_{0.5}\text{O}_{6-\delta}$ in tetragonal space group $I4/mcm$ from powder neutron diffraction after cooling the sample in O_2 . Four phases are used in the refinement in order to accommodate the unusual strain broadening observed in the peaks

T ($^{\circ}\text{C}$)	25	25	25	25
Phase	1	2	3	4
Wt fraction	0.144(2)	0.3860(4)	0.0767(6)	0.0444(6)
a (\AA)	5.5538(2)	5.5541(1)	5.5375(3)	5.5059(2)
c (\AA)	7.8754(3)	7.8415(2)	7.8109(5)	7.8174(7)
Sr 4b (0, 1/2, 1/4)				
U_{iso} (\AA^2)	0.0131(1)	0.0131(1)	0.0131(1)	0.0131(1)
f_{occ}	1.00	1.00	1.00	1.00
(Fe–Mo) 4c (0, 0, 0)				
U_{iso} (\AA^2)	0.00800(9)	0.00800(9)	0.00800(9)	0.00800(9)
f_{occ}	1.00	1.00	1.00	1.00
O1 16k (x, y, 0)				
x	0.2354(2)	0.2354(2)	0.2354(2)	0.2354(2)
y	0.7354(2)	0.7354(2)	0.7354(2)	0.7354(2)
U_{11} (\AA^2)	0.0132(4)	0.0132(4)	0.0132(4)	0.0132(4)
U_{22} (\AA^2)	0.0132(4)	0.0132(4)	0.0132(4)	0.0132(4)
U_{33} (\AA^2)	0.0174(7)	0.0174(7)	0.0174(7)	0.0174(7)
f_{occ}	1.00	1.00	1.00	1.00
O2 4a (0, 0, 1/4)				
U_{11} (\AA^2)	0.023(1)	0.023(1)	0.023(1)	0.023(1)
U_{22} (\AA^2)	0.023(1)	0.023(1)	0.023(1)	0.023(1)
U_{33} (\AA^2)	0.007(1)	0.007(1)	0.007(1)	0.007(1)
f_{occ}	1.00	1.00	1.00	1.00
χ^2	7.511	7.511	7.511	7.511
R_p (%)	3.52	3.52	3.52	3.52
R_{wp} (%)	2.65	2.65	2.65	2.65
Distances (\AA)				
Fe–Mo–O1 (x_4)	1.9669(1)	1.9670(1)	1.9611(1)	1.9500(1)
Fe–Mo–O2 (x_2)	1.9689(1)	1.9604(1)	1.9527(1)	1.9544(2)
Average Fe–Mo–O	1.9676(2)	1.9648(2)	1.9583(2)	1.9515(3)
Angles ($^{\circ}$)				
O1–Fe/Mo–O1	90.000	90.000	90.000	90.000
O1–Fe/Mo–O2	180.000	180.000	180.000	180.000
O1–Fe/Mo–O2	90.000	90.000	90.000	90.000
O2–Fe/Mo–O2	180.000	180.000	180.000	180.000

weaker Fe–O bonds that can be readily broken. Therefore, it was predicted by theory that the oxygen vacancies form mostly on the oxygen site between adjacent iron atoms. This was later confirmed by the analysis of powder neutron diffraction data on the low temperature tetragonal structure.¹⁵ In the low temperature tetragonal structure, two oxygen positions can be refined and in cases where that phase is oxygen deficient, the vacancies are located on the O1 site (which is the oxygen site between neighboring iron atoms). The locations of O1 and O2 in the tetragonal $\text{Sr}_2\text{Fe}_{1.5}\text{Mo}_{0.5}\text{O}_{6-\delta}$ structure are indicated in Fig. 1 where the two oxygen positions are colored red and orange, respectively. Of course, in the high temperature cubic structure, there is only one crystallographic oxygen position that can be refined. Nonetheless, there will still be oxygens between two adjacent iron atoms and oxygens between iron and molybdenum atoms and theory predicts that oxygens of the former type are the ones removed to create the oxygen deficient structure. We cannot, however, distinguish between them in the high temperature measurements, although we can readily quantify the number of oxygen vacancies that are created when $\text{Sr}_2\text{Fe}_{1.5}\text{Mo}_{0.5}\text{O}_{6-\delta}$ is heated in either oxygen or hydrogen, as shown in Fig. 6.

To represent the information gathered from neutron diffraction-based structural and compositional data, and from physical property measurements, we have constructed Scheme 1, which illustrates structural changes, oxygen content, and associated electronic and ionic conductivity as a function of temperature and of oxygen partial pressure. The data are all in very good agreement and reveal a nice correlation between the structural and compositional features (location and amount of oxygen vacancy formation) with the physical property measurements (ionic and total conductivity). As the temperature is increased, both in wet oxygen or wet hydrogen, oxygen vacancies are formed that enhance both the oxide ion conductivity as well as the total conductivity *via* the processes identified by published DFT calculations. This represents a most

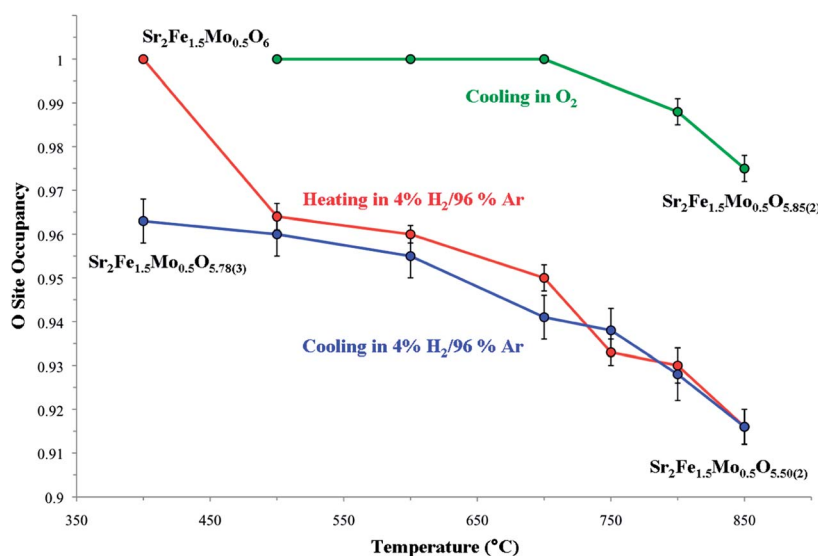
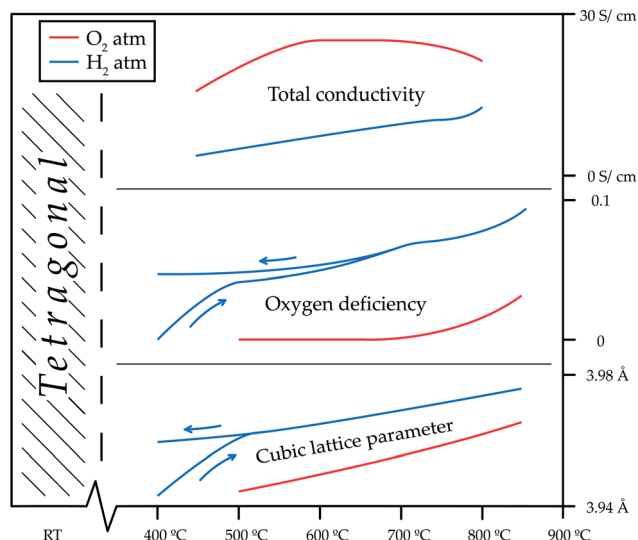


Fig. 6 Plot of O site occupancy versus temperature ($^{\circ}\text{C}$) for $\text{Sr}_2\text{Fe}_{1.5}\text{Mo}_{0.5}\text{O}_{6-\delta}$ on heating in 4% H_2 –96% He (red), cooling in 4% H_2 –96% He (blue), and cooling in O_2 (green), as determined from Rietveld refinements of powder neutron diffraction data.



Scheme 1 Illustration of the relationship between structure, total conductivity, oxygen deficiency and lattice parameter plotted as a function of temperature.

comprehensive description of $\text{Sr}_2\text{Fe}_{1.5}\text{Mo}_{0.5}\text{O}_{6-\delta}$ in different operating environments and, specifically, establishes the structure property correlations therein.

4 Conclusions

The structures and oxygen contents of $\text{Sr}_2\text{Fe}_{1.5}\text{Mo}_{0.5}\text{O}_{6-\delta}$ were determined by variable temperature, variable $p\text{O}_2$, *in situ* powder neutron diffraction experiments. The room temperature tetragonal structure undergoes a phase transition to cubic symmetry by 400 °C and remains cubic to at least 850 °C. Oxygen loss occurs on heating the sample in a wet hydrogen atmosphere, which stems from the creation of vacancies that theory predicts to be located between two iron centers. On cooling the sample in wet hydrogen, the vacancies re-fill, a process that is not complete until the sample temperature reaches room temperature. Similarly, heating the sample to 850 °C under a wet oxygen atmosphere creates vacancies, which refill by 675 °C on cooling. The structure undergoes a phase transition from cubic back to tetragonal below 500 °C. The creation of oxygen vacancies, as predicted by theory, is in excellent correlation with the ionic and the total conductivity.

Acknowledgements

This work was supported as part of HeteroFoaM, an Energy Frontier Research Center funded by the U.S. Department of Energy, Office of Science, and Office of Basic Energy Sciences under Award Number DE-SC0001061. Portions of this research at the Oak Ridge National Laboratory's SNS were sponsored by the Scientific User Facilities Division, Office of Basic Energy Sciences, U.S. Department of Energy. Travel to Oak Ridge National Laboratory to carry out this work was supported by a Travel Fellowship from the DOE-EPSCoR Grant to the University of Tennessee, DE-FG02-08ER46528.

References

- 1 A. J. Jacobson, *Chem. Mater.*, 2010, **22**, 660.
- 2 S. Suthirakun, G. Xiao, S. C. Ammal, F. Chen, H.-C. zur Loye and A. Heyden, *J. Power Sources*, 2014, **245**, 875.
- 3 B. Zhu, *Int. J. Energy Res.*, 2009, **32**, 1126.
- 4 Y.-H. Huang, R. I. Dass, Z.-L. Xing and J. B. Goodenough, *Science*, 2006, **312**, 254.
- 5 Y.-H. Huang, R. I. Dass, J. C. Denysyn and J. B. Goodenough, *J. Electrochem. Soc.*, 2006, **153**, A1266.
- 6 Q. Liu, G. L. Xiao, T. Howell, T. Reitz and F. Chen, *ECS Trans.*, 2011, **35**, 1357.
- 7 G. Xiao, Q. Liu, F. Zhao, L. Zhang, C. Xia and F. Chen, *J. Electrochem. Soc.*, 2011, **158**, B455.
- 8 Q. Liu, X. Dong, G. Xiao, F. Zhao and F. Chen, *Adv. Mater.*, 2010, **22**, 5478.
- 9 J. H. Wright, A. V. Virkar, Q. Liu and F. Chen, *J. Power Sources*, 2013, **237**, 13.
- 10 G. Xiao, Q. Liu, S. Nuansaeng and F. Chen, *ECS Trans.*, 2012, **45**, 355.
- 11 G. Xiao, Q. Liu, S. Wang, V. G. Komovokis, M. D. Amiridis, A. Heyden, S. Ma and F. Chen, *J. Power Sources*, 2012, **202**, 63.
- 12 Q. Liu, D. E. Bugaris, G. Xiao, M. Chmara, S. Ma, H.-C. zur Loye, M. D. Amiridis and F. Chen, *J. Power Sources*, 2011, **196**, 9148.
- 13 J. Canales-Vazquez, J. C. Ruiz-Morales, D. Marrero-Lopez, J. Pena-Martinez, P. Nunez and P. Gomez-Romero, *J. Power Sources*, 2007, **171**, 552.
- 14 B. He, L. Zhao, S. Song, T. Liu, F. Chen and C. Xia, *J. Electrochem. Soc.*, 2012, **159**, B619.
- 15 M. Retuerto, M.-R. Li, Y. B. Go, A. Ignatov, M. Croft, K. V. Ramanujachary, J. Hadermann, J. P. Hodges, R. H. Herber, I. Nowik and M. Greenblatt, *Inorg. Chem.*, 2012, **51**, 12273.
- 16 A. A. Markov, I. A. Leonidov, M. V. Patrakeev, V. L. Kozhevnikov, O. A. Savinskaya, U. V. Ancharova and A. P. Nemudry, *Solid State Ionics*, 2008, **179**, 1050.
- 17 G. Y. Liu, G. H. Rao, X. M. Feng, H. F. Yang, Z. W. Ouyang, W. F. Liu and J. K. Liang, *J. Alloys Compd.*, 2003, **353**, 42.
- 18 C. Meneghini, S. Ray, F. Liscio, F. Bardelli, S. Mobilio and D. D. Sarma, *Phys. Rev. Lett.*, 2009, 046403.
- 19 A. B. Munoz-Garcia, D. E. Bugaris, M. Pavone, J. P. Hodges, A. Huq, F. Chen, H.-C. zur Loye and E. A. Carter, *J. Am. Chem. Soc.*, 2012, **134**, 6826.
- 20 F. Tonus, C. Greaves, H. El Shinawi, T. Hansen, O. Hernandez, P. D. Battle and M. Bahout, *J. Mater. Chem.*, 2011, **21**, 7111.
- 21 R. A. Cox-Galhotra, A. Huq, J. P. Hodges, J.-H. Kim, C. Yu, X. Wang, A. J. Jacobson and S. McIntosh, *J. Mater. Chem. A*, 2013, **1**, 3091.
- 22 C. N. Munnings, R. Sayers, P. A. Stuart and S. J. Skinner, *Solid State Ionics*, 2012, **14**, 48.
- 23 A. C. Larson and R. B. von Dreele, *General Structure Analysis System (GSAS)*, Los Alamos National Laboratory, Los Alamos, NM, 1990.
- 24 B. H. Toby, *J. Appl. Crystallogr.*, 2001, **34**, 210.
- 25 V. M. Goldschmidt, *Naturwissenschaften*, 1926, **21**, 477.
- 26 M. W. Lufaso, P. W. Barnes and P. M. Woodward, *Acta Crystallogr., Sect. B: Struct. Sci.*, 2006, **62**, 397.